Morphology transitions in bilayer spinodal dewetting systems

S. Yadavali,[1] H. Krishna,[2] and R. Kalyanaraman[1,3,4]

[1]*Department of Chemical & Biomolecular Engineering, University of Tennessee, Knoxville, Tennessee 37996, USA*

[2]*Department of Physics, Washington University in St. Louis, Missouri 63130, USA*

[3]*Department of Materials Science and Engineering, University of Tennessee, Knoxville, Tennessee 37996, USA*

[4]*Sustainable Energy Education & Research Center, University of Tennessee, Knoxville, Tennessee 37996, USA*

(Received 5 March 2012; revised manuscript received 10 May 2012; published 22 June 2012)

In spontaneous pattern formation by spinodal dewetting, attractive intermolecular forces overcome surface tension and cause an ultrathin liquid film on a low energy substrate to produce ordered structures. Spinodal dewetting in single-layer film on a substrate is usually manifested by an early stage surface deformation and a highly nonlinear ripening stage that results in characteristic morphologies, typically bicontinuous- or holelike states. Here we have experimentally constructed the dewetting morphology phase diagrams for a bilayer (Ag, Co) liquid film system on SiO_2. Nanosecond pulsed laser melting was used to initiate and foster the dewetting as a function of film thickness and arrangement. The early stage ripening morphology was observed by scanning electron microscopy from which the phase diagrams were constructed. Unlike single-layer films, which only show one morphology transition between the bicontinuous to hole states as the film thickness is increased, the bilayer system can have multiple transitions. We have utilized the thickness-dependent free energy curvature approach [Sharma and Khanna, Phys. Rev. Lett. **81**, 3463 (1998)] to analyze the phase diagram. The location of the multiple transitions cannot be predicted from the curvature minima, as was the case for single-layer films. Nevertheless, despite the complexity from multiple interacting forces and different surface deformation mode in bilayer systems, the phase diagram can be completely generated by knowledge of the free energy curvature of the respective single-layer films. These results can permit improved modeling of the nonlinear dynamics in naturally driven self-organized phenomenon and help design nanomaterials for advanced applications.

DOI: 10.1103/PhysRevB.85.235446 PACS number(s): 81.07.−b, 68.08.Bc, 64.75.Yz, 61.25.Mv

I. INTRODUCTION

The study of the behavior of self-organizing processes, which appear in systems ranging from geographical to nanoscale sizes, is of fundamental interest because it sheds light on the relationship between the various intrinsic forces and the resulting unique ordered shapes, structures, and morphologies. A well-known example of this is the behavior of diblock copolymer thin films.[1,2] In these systems, thermodynamic immiscibility between the two blocks lead to self-organized structures with lamellar, cubic, or other arrangements, such that the contact between similar and dissimilar components are maximized and minimized, respectively. Since the resulting attributes of size, shape, and arrangement define the various functionalities of the material, the study of such behavior is of considerable practical significance. One naturally occurring process that is broadly applicable to polymer and nonpolymer systems, like metals, is self-organization by dewetting.[3–8] In dewetting a liquid or solid film in contact with a surface spontaneously breaks up due to internal forces to form features with well defined size and shape. However, unlike the case of diblock copolymers, where energy minimization leads to good understanding of the patterns, the behavior of dewetting systems requires a dynamical approach.[9–11]

Over the past 50 years, spontaneous dewetting has been studied quite extensively, especially in single-layer films on a substrate. Current understanding divides dewetting into two categories. One is spinodal dewetting, which leads to structures with spatially ordered features, and hence is of substantial interest.[5–9] The other is nucleation and growth, in which the film overcomes an energetic barrier in its pathway to the deformed state, which may or may not consist of ordered features.[4,12] An important characteristic of spinodal dewetting systems is that the free energy of the film, as a result of the attractive and repulsive surface and intermolecular forces, shows the negative curvature reminiscent of spinodal phase segregating systems.[3,13] Spinodal dewetting proceeds by an early stage perturbation of the initially flat film that selects a preferred length scale, and one which can be well explained by simple linear theories.[3] However, the subsequent evolution or ripening of the film shape, leading to rupture and exposure of the substrate, which is of substantial practical relevance since it controls the visible intermediate stage morphologies, is determined by a complex and highly nonlinear evolution of the film height.[10] Nevertheless, a simplifying theme has been observed in various studies of single-layer film dewetting, in that the early-stage ripening morphology can be quite accurately predicted by the curvature in the film-thickness-dependent free energy $\Delta G(h)$. As first identified by Sharma and Khanna,[11] the position of the minima in the free energy curvature identifies a morphological transition from a bicontinuous stage (to the left of the minima) to a holelike stage (to the right of the minima). The underlying physical reasoning for this behavior is attributed to the role of the free energy curvature in the dynamical equations that determine the transport of matter, much like the case of spinodal phase segregating systems.[14] While the general validity of this observation has been verified in single-layer polymer[15,16] and metal films,[17,18] its applicability to describing the behavior of more complex bilayer films or higher order spinodal dewetting systems has not been evaluated thus far.

In this work, we have investigated the morphological phase diagram for spinodal dewetting in bilayer systems,

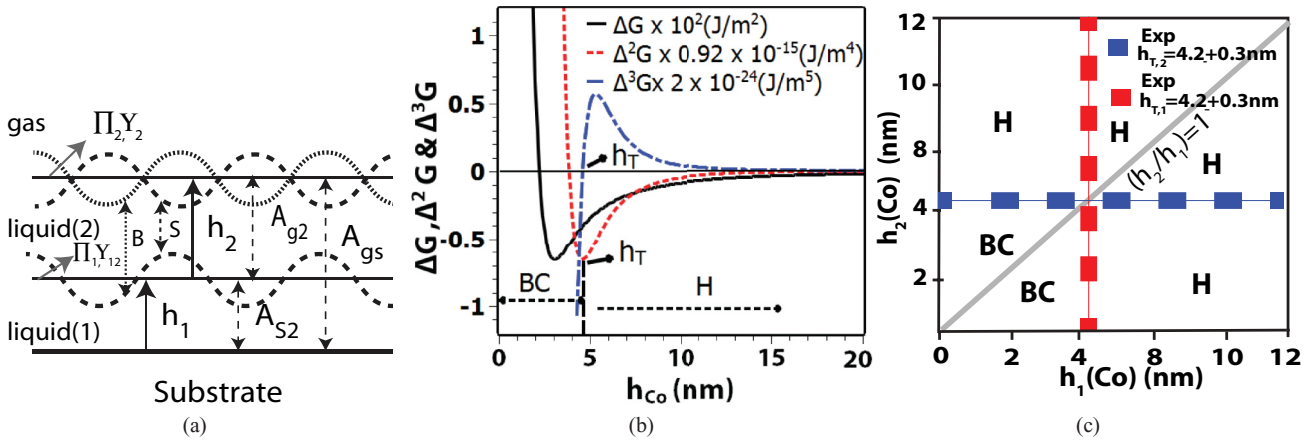

(a) (b) (c)

FIG. 1. (Color online) (a) Schematic description of the geometry and forces in a bilayer dewetting system consisting of two liquids layers on the substrate. Also shown are the two possible types of deformation modes: bending (B) and squeezing (S). The primary interaction forces include the Hamaker coefficients $A_{i,j}$'s between the various pairs of interfaces and the interfacial tension at the film-vacuum and film-film interfaces. (b) The free energy of the Co/SiO_2 system (ΔG), its curvature ($\Delta^2 G$), and the third derivative ($\Delta^3 G$) are shown. The transition thickness h_T corresponds to the minima in the curvature or the zero in the third derivative.[11] (c) Experimentally constructed morphology phase diagram for a single-layer system of Co/SiO_2, which is identical to the bilayer system of Co/Co on SiO_2. The dashed curves are drawn at the location of the morphology transition points for single-layer Co. The thickness of these lines represent the experimental uncertainty in measurement of the transition thickness. Various regions consisting of either bicontinuous (BC) or hole morphologies are shown.

which comprise of two liquid layers (bilayers) on a substrate. As compared to single-layer films, the complexity of the free energy and dynamics in bilayer systems is significantly higher[19–22] than the single layer because of the increase in the pairs of interfaces (three in bilayers vs one in single layer) and the possibility for deformation to occur via bending and squeezing modes, as shown in Fig. 1(a), which are absent in single-layer films. As a prototypical system, we have studied bilayers of metallic liquid films of Co and Ag on a low energy SiO_2 surface. Because of the minimal chemical interactions between the various components, this system provides a good way to explore spinodal dewetting in noninteracting systems, as previously confirmed from the behavior of patterning lengths.[23] In addition, the nanoparticle structures of the final stable state predicted by the nonlinear modeling of this system[24] suggest potential applications in energy harvesting and sensing as bimetallic materials.[25–29] Nanosecond pulsed laser dewetting experiments were performed to generate the early-stage ripening morphology as a function of the thickness and arrangement of the two liquid layers. From this we could construct the phase diagram and determined that only two distinct morphologies are evident—bicontinuous (BC) structures and holes (H)—similar to the single-layer case. We also determined that the bilayer system can show single or multiple transitions between these morphologies with changing film thickness. The bilayer free energy curvature accurately predicted the location of the first morphology transition, much like the single-layer case, but did not predict the second. However, interestingly, the entire bilayer morphology and both transitions can be accurately predicted by the behavior of the two single-layer films, and in this regard, the curvature argument is still a valid one. The implication of this finding is that, despite the vastly more complex length scaling and nonlinear evolution behavior of the bilayer systems, its ripening morphology follows a simple underlying principle.

II. EXPERIMENT AND RESULTS

A. Sample preparation

A detailed description of the preparation of a bilayer system made from Ag and Co on SiO_2 substrates has been published previously.[23] Briefly, ultrathin films of Ag and Co were deposited under ultrahigh vacuum ($\sim 1 \times 10^{-8}$ Torr) by electron beam evaporation (e-beam) and pulsed laser deposition (PLD), respectively, on commercially available and optically smooth 400 nm SiO_2 on Si(100) wafers. The deposition rate for each metal was typically 0.3–0.5 nm/min. Two types of bilayer systems were investigated. In the AgCo system, a bottom Co film was deposited on the substrate, followed by the deposition of a top Ag layer, with total film thicknesses varying from 2 to 20 nm. For the CoAg system, a bottom Ag layer was deposited followed by deposition of the top layer Co film, with total thicknesses varying from 2 to 20 nm. Following the deposition, the films were irradiated in vacuum by a fixed number of pulses n (typically of order 10) from a 266 nm ultraviolet laser having a pulse width τ_p of 9 ns and a Gaussian spatial profile. Irradiation was at normal incidence with an unfocused laser beam of area 1×1 mm^2 at a repetition rate of 50 Hz. The laser energy density was typically between 80 and 100 mJ/cm^2, and chosen such that the entire bilayer could be melted for all the thickness combinations, as evidenced by a visible morphology change.[17,30] The morphology was studied as a function of the individual and combined film thickness of the bilayer systems. The morphology was characterized using a Hitachi S-4300 scanning electron microscope (SEM).

B. Morphology and transition observations

A typical bilayer system is depicted in Fig. 1(a) with the various interfacial and dispersive intermolecular forces

TABLE I. Various possible bilayer cases based on the values of the individual film thickness and their relation to the single-layer transition thickness.

Case	Bilayer system specification	Case	Bilayer system specification
1	$(h_2 < h_1; h_2 < h_{T,2}; h_1 < h_{T,1})$	5	$(h_2 > h_1; h_2 < h_{T,2}; h_1 > h_{T,1})$
2	$(h_2 > h_1; h_2 < h_{T,2}; h_1 < h_{T,1})$	6	$(h_2 > h_1; h_2 > h_{T,2}; h_1 > h_{T,1})$
3	$(h_2 > h_1; h_2 > h_{T,2}; h_1 < h_{T,1})$	7	$(h_2 < h_1; h_2 > h_{T,2}; h_1 > h_{T,1})$
4	$(h_2 < h_1; h_2 < h_{T,2}; h_1 > h_{T,1})$	8	$(h_2 < h_1; h_2 > h_{T,2}; h_1 < h_{T,1})$

between the layers and the two general modes of deformations: bending (B) or squeezing (S). Based on the experimental observations from SEM imaging to be discussed shortly, the bilayer systems could be classified into eight distinct cases, as shown in Table I, on the basis of the thickness of the individual films in relation to each other and in relation to the single-layer transition thickness $h_{T,1}$ and $h_{T,2}$. As reported previously, the $h_{T,\mathrm{Co}}$ for single-layer Co on SiO_2 is ~4 nm,[31,32] while the $h_{T,\mathrm{Ag}}$ for Ag on SiO_2 film was found to be ~10.5 nm.[17] Guided by these experimental values, we evaluated the morphology for the two systems via SEM analysis as shown in Fig. 2, which denote the early-stage ripening morphology for different representative cases of the AgCo and CoAg bilayer systems. Each SEM image was evaluated for the short range spatial order that is consistent with spinodal dewetting. This was done by obtaining the fast Fourier transform (FFT) of the SEM image contrast, which is shown in the inset of each SEM image. The FFT's showed the characteristic annular form, which is indicative of a narrow band of characteristic length scales for the height variations on the surface.[4,12,33] The primary information conveyed by this set of SEM images is the two distinctly different types of morphologies: the bicontinuous structures in Figs. 2(a), 2(b), 2(e), and 2(h) and the hole structures in Figs. 2(c), 2(d), 2(f), and 2(g), analogous to the situation with single-layer films.[11,17] These were the only two observed bilayer morphologies, besides a mixed state that comprised both morphologies which occurred when the bilayer systems were at the positions of morphological transitions. In subsequent analysis and discussions we only distinguish between the type of patterns, i.e., BC or H. Any change between BC and H or vice versa will be referred to as a phase transition, while any changes between similar morphologies but accompanied by a change in length scale of the pattern as film thickness was varied was not considered as a phase transition (and is rather a pseudotransition).

1. AgCo system

In Fig. 2(b) the early-stage morphology is shown for the Ag(5 nm)/Co(3 nm) bilayer, which is for the case in which both films are less than their individual transition thickness, corresponding to case 2 in Table I. The top Ag layer thickness was varied from $(4\,\mathrm{nm} < h_{\mathrm{Ag}} < h_{T,\mathrm{Ag}})$ on the bottom Co layer of 3 nm thickness. The morphology progression is through formation of *bicontinuous* (BC) structures, which is the morphology behavior of a single silver or cobalt layer on the substrate. In Fig. 2(d) the progression of morphology is shown for the Ag(4 nm)/Co(5 nm) bilayer, which is for the case in which the top Ag layer thickness varied from $(1 < h_{\mathrm{Ag}} < 5\,\mathrm{nm})$ on a bottom Co layer of 5 nm, corresponding to case 4 in Table I. The morphology progression is through formation of *holes (H),* which is the morphology behavior of a single cobalt layer with $h_{\mathrm{Co}} = 5$ nm on the substrate. In Fig. 2(e) the progression of morphology is shown for the Ag(6 nm)/Co(5 nm) bilayer, which is for the case in which the top Ag layer thickness was varied from $(5\,\mathrm{nm} < h_{\mathrm{Ag}} < h_{T,\mathrm{Ag}})$ on a bottom Co 5 nm film, corresponding to case 5 in Table I. The morphology progression is through formation of BC structures which is the morphology behavior of a single silver layer on a substrate. In Fig. 2(f) the progression of morphology is shown for the Ag(12 nm)/Co(5 nm) bilayer, which is for the case in which both films are greater than their individual transition thickness, corresponding to case 6 in Table I. The top Ag layer thickness was varied as $(h_{\mathrm{Ag}} > h_{T,\mathrm{Ag}})$ on a bottom Co 5 nm film. The morphology progression is through formation of *H,* similar to the behavior of single silver or cobalt films on the substrate.

2. CoAg system

In Fig. 2(a) the progression of morphology is shown for the Co(4 nm)/Ag(5 nm) bilayer, which is for the case in which both films are less than their individual transition thickness.The top Co layer thickness was varied from $(1 < h_{\mathrm{Co}} \leqslant h_{T,\mathrm{Co}})$ on a bottom Ag layer of 5 nm thickness, corresponding to case 1 in Table I. The morphology progression is through formation of BC structures, which is the morphology behavior of individual silver or cobalt layers on the substrate. In Fig. 2(c) the progression of morphology is shown for the Co(6 nm)/Ag(5 nm) bilayer, which is for the case in which the top Co layer of thickness $h_{\mathrm{Co}} > 5$ nm was deposited on a bottom Ag layer of 5 nm thickness, corresponding to case 3 in Table I. Now, the morphology progression is through formation of *H,* which is the behavior of a single cobalt layer with h_{Co}>5 nm on the substrate. In Fig. 2(g) the progression of morphology is shown for the Co(7 nm)/Ag(12 nm) bilayer, which is for the case in which the top Co layer was varied from $6\,\mathrm{nm} < h_{\mathrm{Co}} < 13$ nm on the bottom Ag layer of 12 thickness, corresponding to case 7 in Table I. The morphology progression is through formation of *H,* which is the morphology progression of either film if they are greater than their transition thickness. In Fig. 2(h) the progression of morphology is shown for the Co(5 nm)/Ag(8 nm) bilayer, which is for the case in which the top Co layer was varied as $5\,\mathrm{nm} < h_{\mathrm{Co}} < 9\,\mathrm{nm}$ on the bottom Ag layer of 9 nm thickness, corresponding to case 8 in Table I. The morphology progression is through formation of *BC structures*, which is the morphology behavior of an individual 9 nm silver layer.

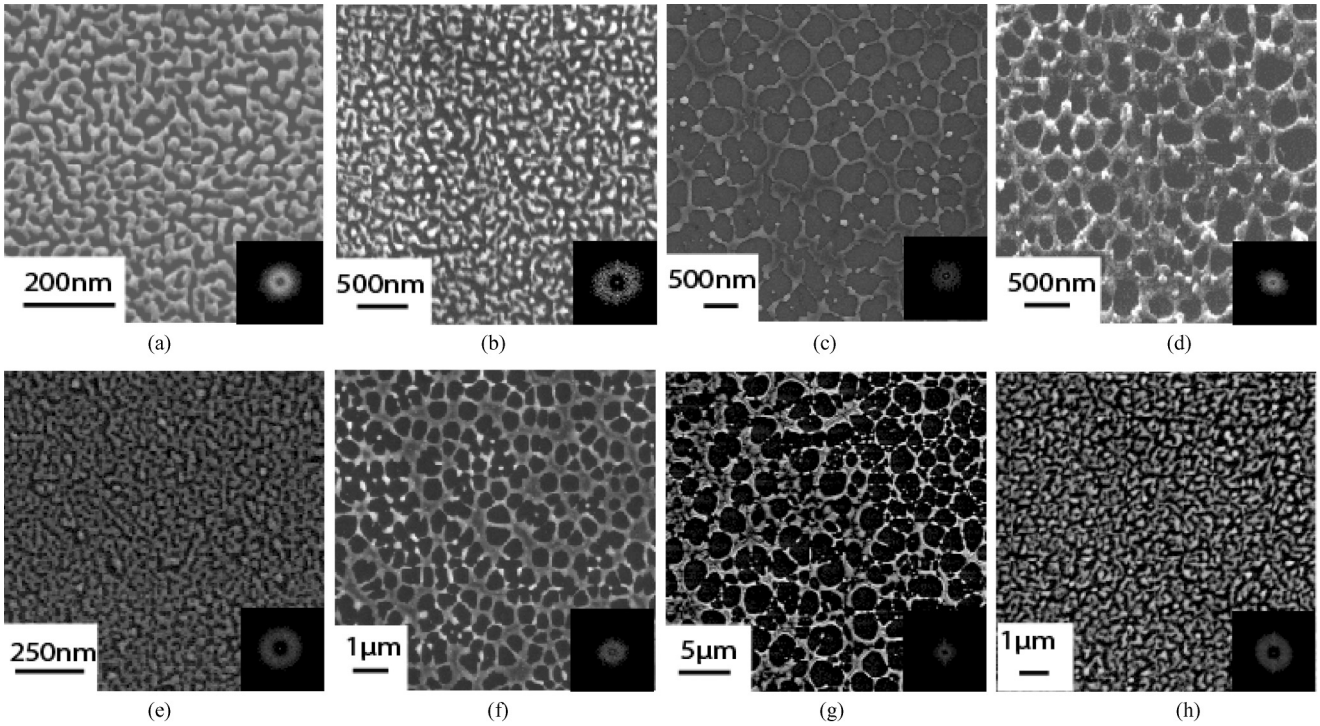

FIG. 2. SEM images of the early stage spinodal dewetting morphologies in bilayer dewetting systems. The film thickness from (a) to (h) correspond as follows: (a) Co(4 m)/Ag(5 nm) corresponds to case 1, (b) Ag(5 nm)/Co(3 nm) corresponds to case 2, (c) Co(6 nm)/Ag(5 nm) corresponds to case 3, (d) Ag(4 nm)/Co(5 nm) corresponds to case 4, (e) Ag(6 nm)/Co(5 nm) corresponds to case 5, (f) Ag(12 nm)/Co(5 nm) corresponds to case 6, (g) Co(7 nm)/Ag(12 nm) corresponds to case 7, and (h) Co(5 nm)/Ag(8 nm) corresponds to case 8. All cases are described in Table I.

III. DISCUSSION

From the collective SEM results of the early-stage morphology, a few general remarks can be made. A single transition is observed if the bottom layer is less than its transition thickness $\left(h_1 < h_{T,1}\right)$ and the top layer is varied such that the thickness range includes the transition thickness $h_{T,2}$. In this system, the morphology transition from bicontinuous to holes occurs exactly at the top layer transition thickness, i.e., at $h_{2,T}$. If both layers of the bilayer system were greater than their individual transition thickness, the progression of morphology is through *holes* and is evident from SEM images in Figs. 2(f) and 2(g). On the other hand, if both layers were less than their transition thickness the progression of morphology is through bicontinuous structures and is evident from the SEM image in Fig. 2(b). Finally, if both films were of equal thickness and if one film is greater than its transition thickness, a combination of holes and bicontinuous structures was observed. On the other hand, multiple morphology transitions are observed when $h_1 > h_{T,1}$ and $h_{2,T} > h_{T,1}$, and the top layer is varied as $(1 < h_2 < h_{2,\max})$, where $h_{2,\max} > h_{T,2}$. In other words, here the morphology progression will begin with holes for $h_2 < h_1$, transition to bicontinuous structures at $h_1 < h_2 < h_{T,2}$, and then transition to holes at $h_2 = h_{T,2}$. This feature can be observed in the AgCo system, since $(h_{\mathrm{Ag},T} > h_{\mathrm{Co},T})$ and is evident from the SEM images in Figs. 2(d)–2(f). Based on these results, we have constructed the bilayer phase diagram, discussed next.

A. Construction of bilayer phase diagram

The experimentally constructed phase diagram for the AgCo is shown in Fig. 3(a) and for the CoAg system in Fig. 3(b). The phase diagram identifies the morphology for any given combination of h_1 and h_2. Individual regions in the diagram are bounded by values of the experimental transition points $h_{T,1}^{\mathrm{expt}}$, $h_{T,2}^{\mathrm{expt}}$, the film thickness ratio line with slope 1 (i.e., $h_2/h_1 = 1$), and the two thickness axis. This construction permits one to easily predict the early stage morphology for any given path and for any given individual thickness of the components of the bilayer system and their arrangement. For instance, in Fig. 3(a), for the AgCo system, a vertical dashed line is drawn beginning at the bottom layer thickness $h_1 = h_{\mathrm{Co}} = 5$ nm and represents the case where the top layer thickness of the bilayer system is varied for a constant bottom layer. For the various positions along this path, the morphology as well as morphology transitions can readily be identified. For instance, in this case, a first morphology transition will occur at the location of the intersection of the line with the $h_2/h_1 = 1$ line and then a second transition will occur at the intersection with the $h_{T,2}$ line. An important result here was that the experimentally observed locations of the transitions, i.e., $h_{T,1}^{\mathrm{expt}}$ and $h_{T,2}^{\mathrm{expt}}$ coincided within experimental uncertainty to the transition thickness of the respective single-layer films, in this case Co and Ag, respectively. It should be reemphasized here that we refer to a phase transition only when there is a change in the type of morphology, i.e., BC and H. There are

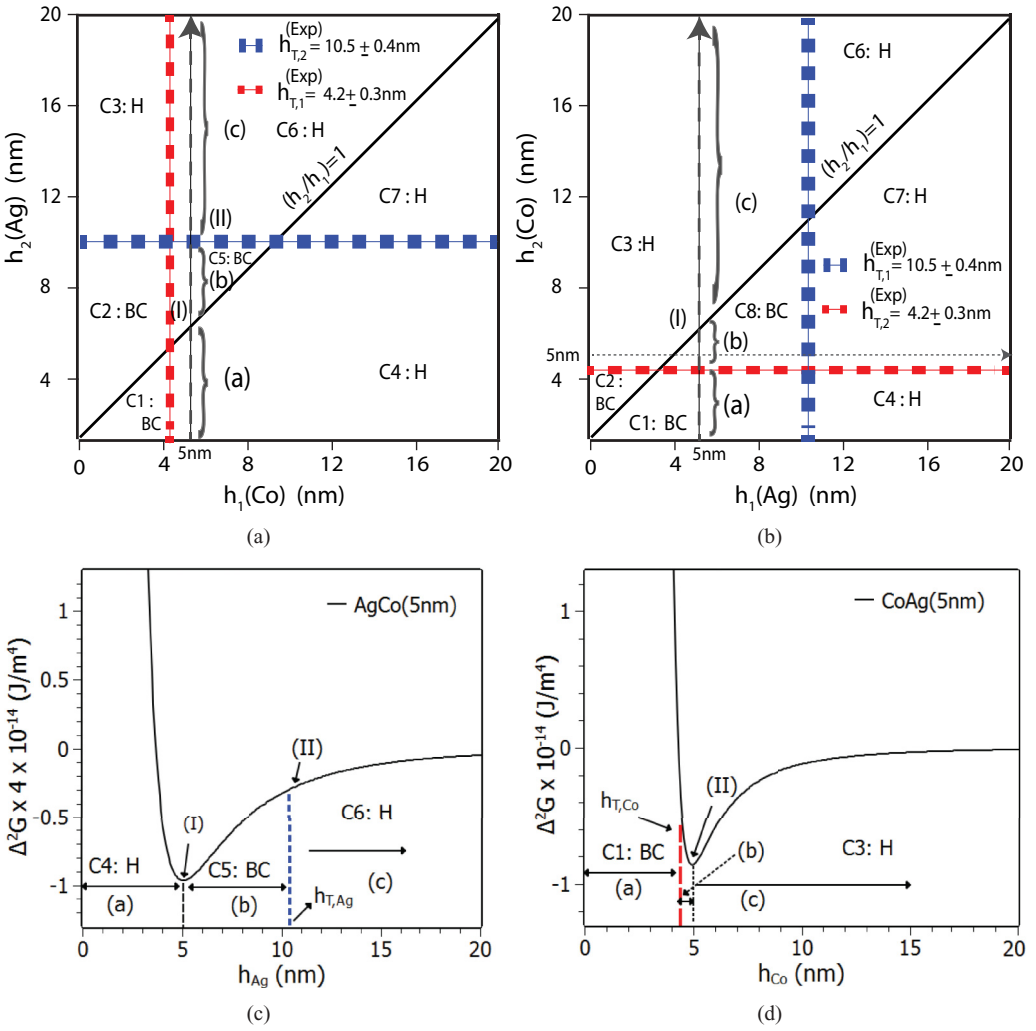

FIG. 3. (Color online) (a) Experimentally generated morphology phase diagram of AgCo system ($h_{T,2} > h_{T,1}$). (b) Phase diagram of CoAg system ($h_{T,2} < h_{T,1}$). (c) Free energy curvature of bilayer AgCo(5 nm) where the red and blue lines correspond to individual Co and Ag transitions. (d) Free energy curvature of CoAg(5 nm) where red and blue lines correspond to individual Co and Ag transitions. The width of the experimentally observed transition lines in (a) and (b) corresponds to the uncertainty in film thickness measurements.

several examples where there can be a change in the length scale of any given morphology, such as the BC or H, when one of the boundaries is crossed. For instance, in Fig. 3(a), there is a change in length scale in going from the case 1 (marked as C1 on the figure) region to the case 2 (C2) region. However, this transition is not a phase transition and, instead, one can refer to it as a pseudophase transition.

In similar fashion, in Fig. 3(b), for the CoAg system, a line drawn at $h_2 = h_{\mathrm{Co}} = 5$ nm and horizontal to the h_1 axis is shown and represents the case where the bottom layer thickness of the bilayer system is varied with a constant top layer. In this example, again multiple transitions are evident at the intersections with the $h_2/h_1 = 1$ line and then with the $h_{T,1}$ position. Once again the experimentally observed locations of the phase transitions coincided within experimental uncertainty to the transition thickness of the respective single-layer systems. Finally, for completeness, we have also constructed the phase diagram for a single layer, which can be thought of as a bilayer with identical liquids, such as Co/Co, in Fig. 1(c). One significant difference in the single-layer behavior over the bilayer case is that only a single morphology transition is possible for any path in the single-layer system.

B. Free energy analysis

In the context of spinodal dewetting, the thickness-dependent free energy $\Delta G(h)$ plays two roles. First, it establishes the "spinodal" nature, i.e., the film thickness range over which the curvature ($\Delta^2 G = \frac{d^2 \Delta G}{dh^2}$) is negative, analogous to spinodal phase segregation. When this condition is satisfied, it is then possible to extract the characteristic length scale of the spinodal system via a linear analysis.[3] Second, as was first shown by Sharma and Khanna,[11] the position of the curvature minima, i.e., where $\Delta^3 G = \frac{d^3 \Delta G}{dh^3} = 0$, identified the location of the transition thickness h_T for single-layer spinodal dewetting. They observed also that bicontinuous structures appear in films whose initial thickness lie to the

left of the curvature minimum h_T, while holes correspond to films with thickness to the right of the minimum. This feature has been subsequently verified in single-layer polymer[15,16] and in single-layer metallic films.[17,18] The underlying physical reasoning of this finding was attributed to the role of the third derivative of the free energy in the mass transport behavior of the film. Based on this curvature argument, we have analyzed the single-layer and bilayer free energies and their derivatives next.

1. Single-layer free energy

Thin film wetting and dewetting behavior is partly determined by the disjoining pressure, which arises from the interaction energies of molecules in a film, which are in close proximity to a surface or interface, being different from that in the bulk. The total disjoining pressure can be written as a combination of long range (Π_l) forces, for example, the van der Waals force, and short range (Π_s) interactions, such as from electrostatic double layers, polar hydrophobic, and other short range repulsions.[34,35] For single-layer metal films, we have previously estimated a total disjoining pressure by considering a long-range attraction, a short-range repulsion expressed as a Lennard-Jones type, and a short range electrostatic force given by[17]

$$\Pi(h) = \frac{A}{h_c^3}\left[\left(\frac{h_c}{h}\right)^3 - \frac{1}{3}\left(\frac{h_c}{h}\right)^9\right] + \frac{S^p}{l}\exp\left(\frac{-h}{l}\right), \quad (1)$$

where A is the Hamaker coefficient, l is the correlation length, S^p is the spreading coefficient, θ is the equilibrium contact angle of the film on the substrate, and h_c is defined as $\frac{A}{h_c^2}\frac{3^{4/3}}{8} = -2\gamma\sin^2(\theta/2)$, where γ is the surface energy of film vacuum interface. Using Eq. (1), the bilayer h_T is calculated from the position of the minimum of free energy curvature ($\frac{d^2\Delta G}{d^2h}$) or where $\frac{d^3\Delta G}{d^3h} = 0$, which is expressed as

$$\frac{d^3\Delta G}{dh^3} = -\frac{12A}{h^5} + \frac{30Ah_c^6}{h^{11}} - \frac{S^p}{l^3}\exp(-h/l) = 0. \quad (2)$$

The above analysis was performed for Co films on an SiO_2 surface (with the various parameters shown in Table II) and the result is shown in Fig. 1(c). The transition thickness h_T is shown at the position where $\frac{d^3\Delta G}{d^3h} = 0$. Experimentally, we observed bicontinuous structures to the left of h_T and holes on the right of the transition thickness and the resulting Co single-layer phase diagram was of the form shown in Fig. 1(c).

TABLE II. Magnitudes of the various parameters used in estimating the free energy and its derivatives for the bilayer and single-layer system.

Parameter	Ag/Co/SiO_2	Co/Ag/SiO_2	Co/SiO_2
A_{s2}	-9.19×10^{-19}	6.07×10^{-19}	A: -3.1×10^{-19}
A_{gs}	-3.95×10^{-18}	-5.23×10^{-19}	h_c: 0.293 nm
A_{g1}	1.01×10^{-19}	-1.04×10^{-19}	γ: 1.882
S^{sr}_{1S2}	-2.07	1.4107	S^p: 2.26
S^{sr}_{21}	-2.43	-2.32	θ: 101
l_0	0.158 nm	0.328 nm	0.458 nm

2. Bilayer system free energy

In order to verify if the morphology phase diagram for the bilayer can also be addressed by the curvature-dependent behavior, we also performed the free energy analysis for the bilayer films. The disjoining pressures acting across the liquid-liquid interface $\Pi_1(h1,h2)$ and liquid-gas interface $\Pi_2(h1,h2)$ can be computed from the forces acting at the interfaces[21] along with short range forces represented as an exponential decay[19,35,36] as follows:

$$\Pi_1(h1,h2) = \frac{A_{s2}}{6\pi h_1^3} - \frac{Ag1}{6\pi(h_2-h1)^3} - \frac{S^{sr}_{1s2}}{l}\exp\left(\frac{d_0-h_1}{l}\right), \quad (3)$$

$$\Pi_2(h1,h2) = \frac{A_{sg}-A_{s2}-A_{g1}}{6\pi h_2^3} + \frac{Ag1}{6\pi(h_2-h1)^3} - \frac{S^{sr}_{21}}{l}\exp\left(\frac{d_0-(h_2-h_1)}{l}\right). \quad (4)$$

The thickness-dependent free energy for the bilayer can now be expressed as

$$\Delta G(h_1,h_2) = \frac{A_{sg}-A_{s2}-A_{g1}}{12\pi h_2^2} + \frac{A_{s2}}{12\pi h_1^2} + \frac{A_{g1}}{12\pi(h_2-h1)^2} - \frac{S^{sr}_{1s2}}{l}\exp\left(\frac{d_0-h_1}{l}\right) - S^{sr}_{21}\exp\left(\frac{d_0-(h_2-h_1)}{l}\right). \quad (5)$$

Here, A_{gs}, A_{s2}, and A_{g1} are the Hamaker coefficients of gas and substrate, substrate and liquid, gas and liquid 1 pair of interfaces, as shown in Fig. 1(a), l is the correlation (or Debye) length, which is typically in the range 0.2–1.0 nm,[35,37] d_0 is the equilibrium cutoff distance taken as 0.158 nm,[35,37] and S^{sr}_{1s2} and S^{sr}_{21} are the short range part of the spreading coefficients. These are also related to the total spreading parameter S of the interface according to Eq. 4 in Ref. 38 as

$$S = S^{vdw} + S^{sr},$$

where S^{vdw} represents the van der Wall's component of spreading coefficient, connected to the effective Hamaker constant via $S^{vdw} = \frac{-A_{\text{effective}}}{12\pi d_0^2}$. Hence

$$S_{1S2} = S^{vdw}_{1S2} + S^{sr}_{1s2} \equiv -\frac{A_{\text{effective}}}{12\pi d_0^2} + S^{sr}_{1S2}. \quad (6)$$

Similarly, S^{sr}_{21} was calculated for both AgCo and CoAg and the bulk spreading coefficients, S_{1S2} and $A_{\text{effective}}$, were calculated from Ref. 20. The various parameters used for the bilayer free energy analysis are shown in Table II. Analogous to the single layer, free energy curvature was estimated from Eq. (7). For a simplified analysis, we held the thickness of the bottom liquid layer fixed, which resulted in the curvature and its derivative

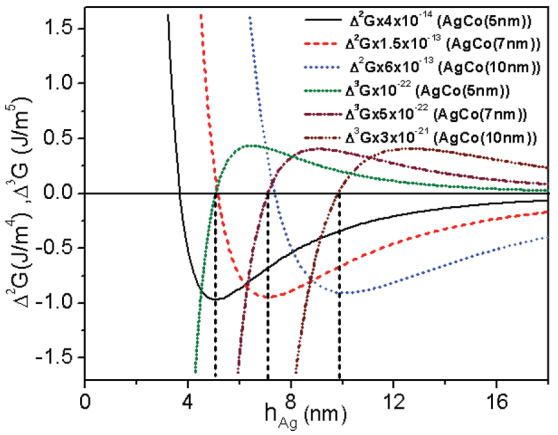

FIG. 4. (Color online) Second ($\Delta^2 G$) and third derivative ($\Delta^3 G$) of the free energy for the AgCo bilayer system for varying values of the bottom Co layer thickness of 5, 7, and 10 nm calculated from Eqs. (7) and (8). The minima in the $\Delta^2 G$ for each case corresponds to the zero in the $\Delta^3 G$ (shown by the vertical dashed line for each case). The location of the zero in $\Delta^3 G$ represents the location of the first transition point in the bilayer dewetting morphology.

being expressed as

$$\Delta^2 G = \frac{\partial^2 \Delta G}{\partial h_2^2} = \frac{Ags - As2 - Ag1}{2\pi h_2^4} + \frac{Ag1}{2\pi (h_2 - h1)^4} - \left(\frac{S_{21}^{sr}}{l^2}\right) \exp\left(\frac{d_0 - (h2 - h1)}{l}\right), \quad (7)$$

$$\Delta^3 G = \frac{\partial^3 \Delta G}{\partial h_2^3} = -2\left(\frac{Ags - As2 - Ag1}{\pi h_2^5}\right) - \frac{2Ag1}{\pi (h_2 - h1)^5} + \left(\frac{S_{21}^{sr}}{l^3}\right) \exp\left(\frac{d_0 - (h2 - h1)}{l}\right). \quad (8)$$

The analysis for evaluating the bilayer transition thickness h_T^{Bi} in a manner analogous to the single-layer case was performed for AgCo(5 nm) as shown in Fig. 3(c) and for CoAg(5 nm) as shown in Fig. 3(d). In addition, the $\Delta^2 G$ and $\Delta^3 G$ for varying bottom Co layer thickness (of 5, 7, and 10 nm) was compared for the AgCo system, as shown in Fig. 4.

3. AgCo morphology behavior

Figures 3(a) and 3(c) show the phase diagram of AgCo bilayer system and free energy curvature for the AgCo(5 nm) system, respectively. We discuss a typical scenario, represented by the dashed vertical line (with ending arrow) drawn on Fig. 3(a) at a bottom layer thickness $h_1 = h_{Co} = 5$ nm. This represents a general case where the top Ag layer thickness of the bilayer system is varied with a constant Co bottom layer of 5 nm. As shown on the phase diagram, this line passes through various morphology regions, denoted by (a), (b), and (c), as well as various morphology transition points, represented by the roman numerals (I) and (II). The two most important results here are that (1) the bilayer system can have multiple morphology transitions, as evidenced at the points I and II, and (2) the morphology at lower thickness can be holes and then change to a bicontinuous state. Both of these features are absent in the single layer, as seen in Fig. 1(c).

The corresponding locations of the regions and points are also indicated on the free energy curvature plot in Fig. 3(c). The immediate result apparent from Fig. 3(c) is that there is only a single minima in the curvature (as quantitatively evidenced from Fig. 4). This means that the bilayer curvature can at most predict only one transition based on the curvature argument and, indeed, the minima corresponds to the first transition at point I. Therefore, the curvature-dependent approach in the bilayer case is only partially able to predict morphology transitions. The conclusion that can be drawn from this analysis is that the bilayer AgCo phase diagram cannot be constructed from a knowledge of the bilayer free energy. On the other hand, as Fig. 3(a) shows, it is possible to easily construct the diagram provided one knows the locations of the single-layer transitions for Ag and Co.

4. CoAg morphology behavior

Figures 3(b) and 3(d) show the phase diagram of CoAg bilayer system and free energy curvature of CoAg(5 nm) system, respectively. As for the AgCo case, a typical scenario is represented by the dashed line drawn at bottom layer thickness $h_1 = h_{Ag} = 5$ nm and vertical to the h_2 axis in Fig. 3(b). This represents the case where the top Co layer thickness of the bilayer system is varied with a constant Ag bottom layer of 5 nm. Once again, on the phase diagram, this line passes through various morphology regions, denoted by (a), (b), and (c), as well as a morphology transition point marked as I. The intersection of regions a and b is a pseudotransition, while b and c corresponds to a phase transition. This bilayer system has a single transition, and the morphology at lower thickness is the bicontinuous state and changes to holes, analogous to the single-layer system, as seen in Fig. 1(c). The corresponding locations of the regions and point are shown in Fig. 3(d). Again only one minima is evident and this corresponds to the location of the transition point marked on the phase diagram. Unlike the AgCo case described in Fig. 3(c), the transition now is from bicontinuous to holes, and this shows the additional uncertainty in utilizing the bilayer free energy curvature in generalizing the morphology on either side of the transition, in contrast to the single-layer system. Once again, we can conclude that the CoAg bilayer curvature cannot predict the phase diagram. However, just as in the case of the AgCo system, as Fig. 3(b) shows, it is possible to easily construct the diagram provided the two single-layer transition points are known.

IV. SUMMARY AND CONCLUSION

We have investigated the early stage ripening morphologies and morphology transitions in bilayer spinodal dewetting systems made from Ag/Co and Co/Ag bilayers on SiO_2 surfaces. By varying the individual film thickness and investigating the dewetting morphology following nanosecond pulse laser melting for various film thickness cases, we have experimentally constructed the phase diagrams for the bilayer dewetting systems. Analogous to single-layer dewetting, the bilayer systems only show either the characteristic bicontinuous or hole like morphologies as a function of varying thickness. However, unlike the single-layer films, multiple morphology transitions may occur. Based on analysis of the free energy curvature, we determined that bilayer systems only partially

follow the curvature minima and morphology relationship found in single-layer films, in which the minima determined the location of the films transition thickness and this was always from a bicontinuous (to the left of the minima) to a holelike (to the right of the minima) morphology. For the bilayer case, the minima represents one of the possible transitions and could either be a bicontinuous to hole or a hole to bicontinuous transition. However, the bilayer phase diagram can be completely described by the location of the two single-layer film transitions that make up the system. Therefore, despite the complexity of the nonlinear evolution of the morphology in bilayer dewetting systems, one can easily construct the complete morphology phase diagram from the behavior of the individual single-layer films. The result can help improve the speed and accuracy of nonlinear modeling of such pattern forming phenomenon and also help to fabricate multielemental nanomaterials with morphologies that could show useful physical properties.

ACKNOWLEDGMENTS

The authors acknowledge support by the Sustainable Energy Education Research Center, and the NSF through Grants No. CMMI-0855949 and No. DMR-0856707.

[1] L. Leibler, Macromolecules **13**, 1602 (1980).
[2] S. B. Darling, Prog. Polym. Sci. **32**, 1152 (2007).
[3] A. Vrij, Discuss. Faraday Soc. **42**, 23 (1966).
[4] P.-G. de Gennes, F. Brochard-Wyart, and D. Quere, *Capillarity and Wetting Phenomenon* (Springer, New York, 2003).
[5] G. Reiter, Phys. Rev. Lett. **68**, 75 (1992).
[6] A. Sharma and E. Ruckenstein, Langmuir **2**, 480 (1986).
[7] S. Herminghaus, K. Jacobs, K. Mecke, J. Bischof, A. Fery, M. Ibn-Elhaj, and S. Schlagowski, Science **282**, 916 (1998).
[8] J. Trice, D. Thomas, C. Favazza, R. Sureshkumar, and R. Kalyanaraman, Phys. Rev. B **75**, 235439 (2007).
[9] C. Redon, F. Brochard-Wyart, and F. Rondelez, Phys. Rev. Lett. **66**, 715 (1991).
[10] J. Becker, G. Grun, R. Seeman, H. Mantz, K. Jacobs, K. Mecke, and R. Blossey, Nat. Mater. **2**, 59 (2003).
[11] A. Sharma and R. Khanna, Phys. Rev. Lett. **81**, 3463 (1998).
[12] T. Stange and D. Evans, Langmuir **13**, 4459 (1997).
[13] A. Vrij and J. T. G. Overbeek, J. Am. Chem. Soc. **90**, 3074 (1968).
[14] R. Desai and R. Kapral, *Dynamics of Self-Organized and Self-Assembled Structures* (Cambridge University Press, Cambridge, UK, 2009).
[15] R. Seemann, S. Herminghaus, and K. Jacobs, J. Phys.: Condens. Matter **13**, 4925 (2001).
[16] R. Xie, A. Karim, J. Douglas, C. Han, and R. Weiss, Phys. Rev. Lett. **81**, 1251 (1998).
[17] H. Krishna, R. Sachan, J. Strader, C. Favazza, M. Khenner, and R. Kalyanaraman, Nanotechnology **21**, 155601 (2010).
[18] S. Strobel, C. Kirkendall, J.-B. Chang, and K. K. Berggren, Nanotechnology **21**, 505301 (2010).
[19] A. Pototsky, M. Bestehorn, D. Merkt, and U. Thiele, J. Chem. Phys. **122**, 224711 (2005).
[20] D. Bandyopadhyay and A. Sharma, J. Chem. Phys. **125**, 054711 (2006).
[21] L. Fisher and A. Golovin, J. Colloid Interface Sci. **291**, 515 (2005).
[22] P. Brochard Wyart, F. Martin, and C. Redon, Langmuir **9**, 3682 (1993).
[23] H. Krishna, N. Shirato, S. Yadavali, R. Sachan, J. Strader, and R. Kalyanaraman, ACS NANO **5**, 470 (2011).
[24] M. Khenner, S. Yadavali, and R. Kalyanaraman, Phys. Fluids **23**, 122105 (2011).
[25] M. Zayats, S. Pogorelova, A. Kharitonov, O. Lioubashevski, E. Katz, and I. Willner, Chem. Eur. J. **9**, 6108 (2003).
[26] M. Seydack, Biosens. Bioelectron. **20**, 2454 (2005).
[27] H. Garcia, R. Sachan, and R. Kalyanaraman, Plasmonics **7**, 137 (2012).
[28] R. Sachan, S. Yadavali, N. Shirato, H. Krishna, V. Ramos, G. Duscher, S. J. Pennycook, A. K. Gangopadhyay, H. Garcia, and R. Kalyanaraman, Nanotechnology **23**, 275604 (2012).
[29] Y. Wang, J. Dosalek, and W. Knoll, Procedia Eng. **5**, 1017 (2010).
[30] C. Favazza, R. Kalyanaraman, and R. Sureshkumar, Nanotechnology **17**, 4229 (2006).
[31] C. Favazza, J. Trice, R. Kalyanaraman, and R. Sureshkumar, Appl. Phys. Lett. **91**, 043105 (2007).
[32] J. Trice, D. G. Thomas, C. Favazza, R. Sureshkumar, and R. Kalyanaraman, Phys. Rev. B **75**, 235439 (2007).
[33] U. Thiele, M. Mertig, and W. Pompe, Phys. Rev. Lett. **80**, 2869 (1998).
[34] H. I. Kim, C. M. Mate, K. A. Hannibal, and S. S. Perry, Phys. Rev. Lett. **82**, 3496 (1999).
[35] J. Israelachvili, *Intermolecular and Surface Forces* (Academic Press, London, 1992), Chap. 11.
[36] A. Sharma, Langmuir **9**, 861 (1993).
[37] R. Khanna, N. Agnihotri, and A. Sharma, *Kinetics of Phase Transitions* (CRC Press, Boca Raton, FL, 2009).
[38] K. Mougin and H. Haidara, Europhys. Lett. **61**, 660 (2003).